Elucidating and manipulating pressure-induced water intrusion–extrusion in tunable hydrophobic Co/Zn bimetallic ZIFs: Roles of pore size and hydrogen bond

Diyi Fang[1], Chuanlei Liu[1], Yu Chen[1], Qilong Peng[1], Kongguo Wu[1], Yuxiang Chen[1], Hao Jiang[1], Yuan Wu[1], Benxian Shen[1], Qiumin Wu[1], Di Wu[2], and Hui Sun[1] (✉)

[1] International Joint Research Center of Green Energy Chemical Engineering, School of Chemical Engineering, East China University of Science and Technology, Shanghai 200237, China
[2] Alexandra Navrotsky Institute for Experimental Thermodynamics, The Gene and Linda Voiland School of Chemical Engineering and Bioengineering, Materials Science and Engineering, and Department of Chemistry, Washington State University, Washington 99163, USA

ABSTRACT

Porous heterogeneous lyophobic systems (HLSs) find potential applications in energy restoring, dissipating, and absorbing. However, the development of controllable HLSs still lacks rational structure design of nanoporous materials matching the molecular sizes of adopted liquids. Besides that, thoroughly understanding the underlying transportation mechanism in the confined nano channels is greatly challenging. In this work, a series of Co/Zn bimetallic zeolitic imidazolate frameworks (ZIFs) with tunable structures were synthesized via regulating the Co to Zn ratios and employed to investigate the intrusion–extrusion of liquid water in confined nanopores. Structural characterizations confirm the heterometallic coordination in the Co/Zn-doped frameworks. Water intrusion–extrusion experiments unlock the relationship between the intrusion pressure and the nanopore size and realize the evolution of the HLSs between molecular spring and shock-absorber. In addition, cycling tests indicate the reversible structure change of Co/Zn ZIFs encountering pressure-induced water intrusion. In combination with molecular dynamics simulations, we present that the water multimers intrude into nanopores of ZIFs in chain-like forms along with dissociation of hydrogen bonds (HBs). Water molecules in the pre-intrusion state exhibit reduced HBs in response to the increase of pressure and linear structure with 1.6–3.0 HBs on average. After transition to the post-intrusion situation, the associative configuration of water tends to exhibit the tetrahedral structure. Herein, we highlight the roles of pore size and HB in synergically dominating the pressure-induced intrusion–extrusion of liquid water in hydrophobic nanopores. Furthermore, the present work can also guide the development of functional guest–host systems based on porous architectures.

KEYWORDS

heterometallic, zeolitic imidazolate frameworks, nanopore, intrusion, hydrogen bonds

1 Introduction

Nanoporous materials have been finding extremely wide applications in adsorption, separation, catalysis, energy storage, biomedicine, and electronics [1–6], owing to their abundant, uniform and tunable pore structure, and modifiable interfacial properties. Successful applications largely depend on the transportation, diffusion, and complex interactions of guest species confined in diverse porous architectures.

The porous heterogeneous lyophobic system (HLS) [7], for the first time, enabled energy uptake and release in the form of liquid intrusion–extrusion in porous solid materials. Furthermore, the applications of porous materials are extended to the fields of vibration isolation [8] and energy absorption [9]. Owing to their unique nanopore structures and surface functional groups, a number of porous materials having low interfacial affinity to fluids were employed for this purpose. The bulk fluid can only enter the nano channels upon additionally increasing the hydrostatic pressure, resulting in a conversion of mechanical energy to surface

energy [10]. In terms of the potential applications in energy restoring, dissipating, and absorbing, the HLSs can be defined as molecular spring, shock absorber, and bumper [11], respectively.

The mechanical behavior exhibited by HLS strongly depends on the intrusion–extrusion of the pressure-transfer medium in the nanopores, while the transportation of medium is in turn influenced by both the pore structures of frameworks and the nature of the adopted fluids [12–16]. Water has been the most widely employed as a non-infiltrating liquid to study the intrusion–extrusion in regard to diverse porous materials, including silica [17–19], zeolites [20–23], and metal-organic frameworks (MOFs) [24]. Zeolitic imidazolate frameworks (ZIFs), firstly reported by Yaghi and his coworkers [25], typically consist of transition metal ions (i.e., Zn^{2+} and Co^{2+}) and N-containing imidazole or imidazole-derived ligands interconnected to form the topological frameworks. Therefore, they can be more flexible by adjusting the compositions of metal ions or organic ligands to construct plentiful structures and provide much higher porosity as

compared to most of the porous infrastructures [26]. As a result, ZIFs can be expected to exhibit a favorable intrusion pressure while maintaining a high energy absorption density [24]. ZIF-8, a sodalite (SOD) topological structure having Zn coordination with 2-methylimidazole, shares six annular pores having a size of 3.4 Å and the 8-membered facets cavity with a diameter of 11.6 Å. The first attempt to study water intrusion into ZIF-8 was made by Ortiz [27]. It was found that the system involving ZIF-8 exhibited lower stiffness coefficient, shear, and Young's modulus as compared to the silica or zeolite systems. These properties of ZIF-8 endow the HLS with great mechanical properties at a rather low pressure. In addition, repeated intrusion–extrusion experiments [28] and high-pressure *in-situ* infrared (IR) characterization [29] confirmed the satisfactory stability of ZIF-8. Using silicone oil as the pressure-transfer medium in combination with the synchrotron X-ray diffraction (XRD) characterization, it was concluded that the structural change of ZIF-8 remains reversible even though undergoing complete amorphization at a high pressure of 28.1 GPa [30]. In a more recent study, the hysteresis in the intrusion–extrusion process of the {ZIF-8+water} system was controlled by adjusting the crystal size as well as the grain arrangement [31]. The combination of *in-situ* neutron scattering and molecular dynamics (MD) simulation revealed that liquid water intrusion could induce a significant expansion of ZIF-8 cage volume [32], while increasing strain rate could improve the critical intrusion energy of the system [33].

However, to the best of our knowledge, all of the investigations were focused on searching for promising porous materials from the previously reported structures via the mechanical property assessments. There is a lack of rational structure design of porous materials in order to match the molecular size of liquid medium, making it unable to precisely tune the intrusion–extrusion of medium in porous materials. Therefore, the mechanical performance is far away from the requirement of ideal HLSs. When water is used as a non-infiltrating liquid of the HLSs, in most cases, the channel aperture is larger than the kinetic diameter of the water molecule (2.7 Å) [34]. Sun et al. [35] reported the intrusion of water into a narrow channel of ZIF-7 with pore size of 2.9 Å at very high pressure (almost 2.3 times higher than that of ZIF-8) owing to the gate-opening effect of this structure. It is worth noting that, unlike water vapor, liquid water consists of multimers formed through strong hydrogen bonds (HBs). As a result, the association state of water molecules determined by hydrogen bonds and the dimension of the nanopores synergistically dominates the complex intrusion–extrusion behavior of liquid water in the hydrophobic porous materials [36, 37]. Paulo et al. [38] confirmed that hydrogen bond formed by the arrangement of water molecules plays an important role in the wetting of secondary channels during water intrusion into zeolite structures with multi-level channels, and the wetting of secondary pores can regulate the wetting of primary pores to affect the intrusion–extrusion of water. Employing molecular dynamics simulations, Bushuev et al. [39] demonstrated that decorating the secondary topological features of the main channels in porous materials can manipulate the interactions among water molecules, stabilize the flow of water intruding into micropores, and therefore adjust the intrusion–extrusion pressure. The development of HLSs requires performance-oriented design and regulation of the nanopore in the light of size of the water multimers rather than the kinetic diameter of single H_2O molecule. Thoroughly understanding the intrusion–extrusion mechanism of the liquid medium in the confined nanopores is fundamentally important to accurately predict the transportation behavior and thus guide the exploration of porous materials, however, still acutely challenging.

In this work, the Co/Zn bimetallic ZIFs having tunable pore

sizes were employed to investigate the intrusion–extrusion of liquid water in nanoporous structures. A series of Co_xZn_{1-x}-$(MeIm)_2$ (MeIm: 2-methylimidazole) samples were synthesized via reaction–diffusion method and their pore sizes were successfully regulated by altering the Co to Zn molar ratio. The mechanical properties of all HLSs of {ZIF+water} were carefully evaluated and the dependence of intrusion pressure on pore size was revealed. In combination with MD simulations, the hydrogen bond-derived association of water molecules in the confined channel under high pressure is theoretically studied via the radial distribution function (RDF) analysis and hydrogen bond calculation. Herein, we highlight the roles of pore size and hydrogen bond in synergically dominating the intrusion–extrusion of liquid water in nanoporous MOFs under high pressure. Furthermore, the present work provides an approach to the rational design and development of functional guest–host systems based on porous architectures.

2 Experimental

2.1 Materials

Zinc nitrate hexahydrate (with > 99.0% purity) was provided by Sinopharm Chemical Reagent Co., Ltd. (Shanghai, China). Cobalt nitrate hexahydrate (with 99.99% purity) and agar (biological reagent) were provided by Shanghai Aladdin Biochemical Technology Co., Ltd. (Shanghai, China). MeIm (with 99.0% purity) was purchased from Meryer Chemical Technology Co., Ltd. (Shanghai, China). N,N-dimethylformamide (DMF) (with > 99.5% purity) was obtained from Shanghai Titan Scientific Co., Ltd. (Shanghai, China). Deionized water was used in all cases. All the chemicals in this study were used as received.

2.2 Synthesis of samples

$Zn(MeIm)_2$ samples were synthesized following a reaction–diffusion method via modifying the previously reported procedure [40]. Reactant I was prepared via dissolving 14.8 g MeIm into a mixture of deionized water and DMF with equal volume. Reactant II was obtained by adding 0.5 wt.% agar into an aqueous solution containing 10.7 g zinc nitrate hexahydrate. The mixture was heated and stirred until the agar dissolved completely. Then, an equal volume of DMF was added under continuously stirring. The obtained reactant II was kept at room temperature for 2 h to allow complete gelation. Hereafter, the solution of reactant I was poured on the top of the gel of reactant II. The reaction mixture remained at room temperature for 2 days. The white resultant was washed with hot water for 3 times to remove excess agar and separated by centrifugation. At last, the resulting product was dried at 60 °C overnight and at 120 °C for 6 h in an oven.

The synthesis procedure of $Co(MeIm)_2$ was very similar to that of $Zn(MeIm)_2$. During the preparation of reactant II, zinc nitrate hexahydrate was replaced with 10.5 g cobalt nitrate hexahydrate.

A series of Co_xZn_{1-x}-$(MeIm)_2$ samples were synthesized by using mixtures of zinc nitrate hexahydrate and cobalt nitrate hexahydrate with different zinc to cobalt ratios. x equals to 0.1, 0.3, 0.5, and 0.7, representing the molar fractions of cobalt nitrate in the dosage of binary nitrates of Zn and Co. As the proportion of cobalt nitrate increased, the color of the synthesized gel gradually changed from light pink to purple

2.3 Characterizations

Powder XRD patterns were recorded on a Bruker D8 ADVANCE X-ray diffractometer (Bruker AXS Inc., Germany) with Ni-filtered Cu Kα radiation (λ = 1.5418 Å) operated at 40 kV and 40 mA.

The 2θ scanning angle ranged from 5° to 80°, with a step size of 0.02° and scanning rate of 5 °·min⁻¹. Cell parameters and volumes were refined by using a Celref.3 software [41]. The morphologies of samples were analyzed by using a NOVA NanoSEM 450 scanning electron microscopy (SEM; FEI, USA) with an accelerating voltage of 15 kV and a beam current of 10 nA. Element analyses were carried out on a Falcon energy-dispersive X-ray spectroscopy (EDS; EDAX Inc., USA). A sputter coated with a thin layer of platinum was performed to avoid electrostatic forces. Information was collected at different positions to obtain an average elemental composition. Homogeneity was checked using backscattered electron (BSE) imaging. The pore structures of all samples were measured via N_2 adsorption at 77 K conducted on a Micromeritics ASAP 2020 apparatus (Micromeritics Inc., USA). The specific surface area was calculated according to the Brunauer–Emmett–Teller (BET) equation, and the micropore volume and pore size distribution were obtained by using the Horvath–Kawazoe (H–K) and nonlocal density functional theory (NLDFT) method. CO_2 adsorption was also measured at 273 K on a BSD-660M A6M physical absorber (BeiShiDe Instrument Co., Ltd., Beijing, China) and the micropore pore size distribution was calculated by using the Dubinin–Astakhov (DA) equation. Water vapor adsorption experiments were performed at 298 K on a BSD-VVS adsorber (BeiShiDe Instrument Co., Ltd., Beijing, China). Prior to the water vapor adsorption experiment, all samples were degassed at 150 °C for 5 h. The P/P_0 values were given at 0.05, 0.1, 0.15, 0.2, 0.4, 0.6, 0.8, and 0.9. Fourier transform infrared (FTIR) spectroscopic analyses were conducted on a Nicolet 6700 FTIR spectrometer (Thermo Fisher Scientific, USA) in an attenuated total reflection (ATR) mode. Each spectrum was obtained from the acquisition of 105 scans from 4000 to 400 cm⁻¹ with a resolution of 2 cm⁻¹. Inductively coupled plasma-optical emission spectrometer (ICP-OES) analyses were performed on an Agilent 725 ICP-OES full-spectrum direct reading plasma emission spectrometer (Agilent, Inc., USA) with the analysis wavelength of 177–785 nm and optic resolution of 0.009 nm. Prior to testing, the samples were dissolved in nitric acid.

2.4 Quasi-static mechanical measurements

In the quasi-static mechanical experiment, 0.1 g of sample was dispersed into 0.4 mL of deionized water and the suspension was transferred into a custom-made well-sealed stainless steel chamber (see Fig. S1 in the Electronic Supplementary Material (ESM)). Mechanical properties were tested on a YRWT-30E universal testing machine (Shanghai MicroCre Light-machine Technical Co., Ltd., China). Loading was exerted on a piston to compress the volume of the chamber at a constant moving rate of 0.1 mm·min⁻¹. Once the pressure reached its maximum, the unloading stage was performed with a withdrawing movement of piston at a rate of −0.1 mm·min⁻¹ until the piston returned to its original position.

2.5 Computational methods

The crystalline structure of $Zn(MeIm)_2$ was obtained from the Cambridge Structure Database (CSD). To obtain the charge distribution, the repeating fragments in the cell were intercepted for DFT calculations [42]. Using the DMol3 package, the atomic charges of the constituent fragments were derived by the electrostatic potential (ESP) fitting method [43]. Calculation results are shown in Fig. S2, and Tables S1 and S2 in the ESM.

The structure models of Co_xZn_{1-x}-$(MeIm)_2$ were constructed by randomly replacing Zn atoms in an original structure of $Zn(MeIm)_2$ with Co atoms. A mixed force field of DREIDING and UFF was used during both the grand canonical Monte Carlo (GCMC) and MD simulations [44, 45]. Lennard–Jones 12–6 potential was used to calculate the interatomic short-range

interactions and the Lorentz–Berthelot mixing rules were employed to describe the guest–host interactions. In the long-range interactions, the electrostatic potential was calculated by using Ewald summation algorithm with an accuracy of 1.0×10^{-4} kcal·mol⁻¹, and the van der Waals forces were investigated using the atomic summation method with a cutoff at a radius of 11.5 Å. The water molecule was used in the simple point charge (SPC) model [46], and the specific parameters are shown in Table S3 in the ESM.

GCMC simulations were performed to calculate the adsorption capacity of water in a $2 \times 2 \times 2$ cubic cell model of Co_xZn_{1-x}-$(MeIm)_2$. For each adsorption point, 1.0×10^7 calculation steps were first performed for equilibrium and another 1.0×10^7 steps were run for data collection. All adsorption calculations were implemented with Sorption package. Energy minimization was done after introducing certain number of water molecules into these Co_xZn_{1-x}-$(MeIm)_2$ frameworks. MD simulations were then performed in an isothermal isobaric (N, P, T) ensemble at a time step of 1 fs. Using Nosé–Hoover–Langevin for temperature control and Berendsen for pressure control, all the MD simulations were run for 0.5 ns to equilibrate the system. Hereafter, the corresponding equilibrium systems were performed in a subsequent canonical (N, V, T) ensemble for 5.0 ns [47]. Simulation was sampled every 500 steps for RDFs analysis and the details for last 50 ps were collected for analyzing the hydrogen bonding among water molecules. As a control group, a water box containing 500 water molecules ($24 \times 24 \times 27$) was built for the comparison analysis and the calculations were implemented with Forcite program. All computational simulations were performed using the Materials Studio software (Accelrys Inc., USA).

3 Results and discussion

Powder XRD analyses are carried out to examine the crystalline phases of all synthesized samples. The simulated XRD patterns of both $Zn(MeIm)_2$ and $Co(MeIm)_2$ from the CSD are provided for comparison (see Fig. S3 (a) in the ESM). These Co_xZn_{1-x}-$(MeIm)_2$ samples synthesized via the reaction–diffusion method exhibit well-matched diffraction peaks with the simulated patterns of two monometallic ZIF samples. SEM images (see Fig. S4 in the ESM) reveal that all samples have a rhombic dodecahedral morphology with 12 exposed {110} faces [48–51]. Characterization results indicate the crystallographic point group of $\bar{4}3m$, which is in accordance with the cubic space group $I\bar{4}3m$ of $Zn(MeIm)_2$ crystals [52]. The refined cell parameters (see Table S4 in the ESM) indicate that the heterometallic coordination leads to an increase in the cell volume. EDS analysis was performed to evaluate the surface metal compositions of Co_xZn_{1-x}-$(MeIm)_2$ samples. Elemental mapping results based on surface scanning confirm the uniform distributions of Zn and Co in all bimetallic samples (see Fig. S5 in the ESM). Moreover, we determined the Co to Zn molar ratio for each sample via the ICP-OES analysis (see Table S5 in the ESM). From the ICP results, the Co to Zn ratios for $Co_{0.1}Zn_{0.9}$-$(MeIm)_2$, $Co_{0.3}Zn_{0.7}$-$(MeIm)_2$, $Co_{0.5}Zn_{0.5}$-$(MeIm)_2$, and $Co_{0.7}Zn_{0.3}$-$(MeIm)_2$ are 0.083, 0.24, 0.42, and 0.62, respectively. To further confirm the bimetallic structures, we performed FTIR analysis on the Co_xZn_{1-x}-$(MeIm)_2$ samples using an ATR mode. In the ATR-FTIR spectra illustrated in Fig. 1(a), the absorption peaks located at 755, 1145, 1415, and 1584 cm⁻¹ correspond to the out-of-plane, in-plane stretching, and bending vibration modes of the imidazole ring and the stretching vibration mode of the C=N bond, respectively [53–55]. The absorption peak at 992 cm⁻¹ is assigned to the C–N stretching vibration [56]. Additionally, a metal–N absorption peak located at around 420 cm⁻¹ [57] gradually shifts toward higher wavenumbers as the
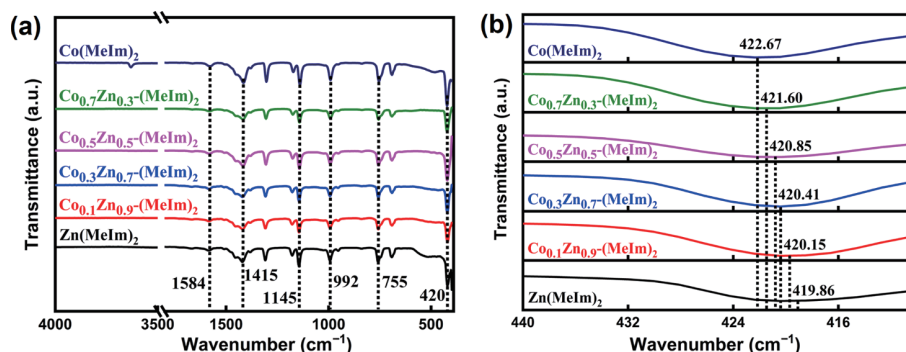
Figure 1 ATR-FTIR spectra of synthesized Co_xZn_{1-x}-$(MeIm)_2$ with wavenumbers ranging (a) from 400 to 4000 cm^{-1} and (b) from 400 to 440 cm^{-1}.

proportion of Co in the framework increases (see Fig. 1(b)). This can be attributed to the higher bonding energy of Co–N (2.834 eV) than that of Zn–N (2.075 eV) [58].

Pore structure data of all samples are obtained via N_2 adsorption measurements at 77 K. The type I isotherms (see Fig. S6(a) in the ESM) indicate that all samples are dominated by microporous structures. Extracted pore structure parameters are listed in Table 1 and the micropore and mesopore size distributions calculated using the NLDFT method are presented in Figs. S6(b) and S6(c) in the ESM. Three types of micropores with sizes of 1.09, 1.19, and 1.30–1.35 nm can be identified from Fig. S6(d) in the ESM. With an increase of Co content, the proportions of the 1.09 nm micropore are 56.94% for $Zn(MeIm)_2$, 57.21% for $Co_{0.1}Zn_{0.9}$-$(MeIm)_2$, 63.11% for $Co_{0.3}Zn_{0.7}$-$(MeIm)_2$, 54.88% for $Co_{0.5}Zn_{0.9}$-$(MeIm)_2$, and 56.18% for $Co_{0.7}Zn_{0.3}$-$(MeIm)_2$, respectively. The micropore of 1.30–1.35 nm accounts for 13.05% for $Zn(MeIm)_2$, 11.04% for $Co_{0.1}Zn_{0.9}$-$(MeIm)_2$, 5.58% for $Co_{0.3}Zn_{0.7}$-$(MeIm)_2$, 8.21% for $Co_{0.3}Zn_{0.7}$-$(MeIm)_2$, and 43.82% for $Co_{0.7}Zn_{0.3}$-$(MeIm)_2$ of the total micropore. The micropores of $Co(MeIm)_2$ have the main size of 1.19 nm. From the pore distribution results, the main mesopores of $Zn(MeIm)_2$, $Co_{0.1}Zn_{0.9}$-$(MeIm)_2$, and $Co(MeIm)_2$ have the size of 4.9 nm. Both $Co_{0.5}Zn_{0.9}$-$(MeIm)_2$ and $Co_{0.7}Zn_{0.3}$-$(MeIm)_2$ have the main mesopore size of 3.8 nm while $Co_{0.3}Zn_{0.7}$-$(MeIm)_2$ has almost no mesopore. The sample having the Co to Zn molar ratio of 3:7 shows the smallest average pore size of 1.48 nm. These results demonstrate that Co doping can change the proportions of the three sizes of micropores to modulate the average micropore size. Furthermore, the accessible surface area (ASA, S_{AC}), probe-occupy volume (POV, V_{PO}), and pore size distribution (see Fig. S7 in the ESM) of the Co_xZn_{1-x}-$(MeIm)_2$ structures were also calculated via using the open software Zeo++ [59] upon Monte Carlo sampling and N_2 as a probe. The calculated pore structure parameters are listed in Table 2. In agreement with the experimental findings, Co doping to $Zn(MeIm)_2$ leads to the increased specific surface area and pore volume. The average sizes of micropores range from 1.01 to 1.14 nm. Additionally, the adsorption isotherms of water vapor on different model structures were obtained via performing the GCMC simulation in order to evaluate the hydrophobicity of these bimetallic materials [60, 61]. Figure S8 in the ESM demonstrates type V adsorption isotherms for all the Co_xZn_{1-x}-$(MeIm)_2$ samples, indicating that water molecules are adsorbed by means of weak interactions. All structures have negligible water uptake at low pressure and sharply increased adsorption at higher relative pressure (above the saturated vapor pressure of water). Specifically, $Zn(MeIm)_2$ exhibits almost no adsorption at the pressure lower than 10 kPa, suggesting its extremely strong hydrophobicity [62]. After doping Co into the framework of $Zn(MeIm)_2$, a remarkable increase in water adsorption can be realized at the pressure of around 1 kPa due to the reduced hydrophobicity of the Co/Zn ZIFs. More interestingly, both the

largest water adsorption and the weakest hydrophobicity can be found at an equivalent dosage of Co and Zn, corresponding to the sample of $Co_{0.5}Zn_{0.5}$-$(MeIm)_2$. Although Co doping reduces the hydrophobicity of the ZIFs, the adsorption results indicate that all samples retain hydrophobic characteristics, thereby preventing the adsorption of water molecules at low pressure. This evidence supports that the synthetic samples can be considered as promising materials for the HLS systems [63].

Furthermore, we evaluated the intrusion–extrusion of liquid water in all the synthesized ZIF samples via quasi-static mechanical measurements. The $P–\Delta V$ curves are presented in Fig. 2(a). All curves can be divided into three regions. During the starting stage, the system exhibits a high stiffness with excellent load-bearing capacity and small volume changes in response to the pressure boost. The second region exhibits a plateau of system pressure, representing the intrusion threshold of water into the nanopores. Therefore, a slight increase in pressure can induce the remarkable water intrusion. As a result, the system exhibits a low stiffness at this stage. In the last region, the pores of the samples are fully filled with water. All systems present high stiffness of the bearing capacity while the $P–\Delta V$ curves have larger slopes than those of the first region. The characteristic parameters extracted from the $P–\Delta V$ curves are summarized in Table 3. The intrusion pressure (P_{in}) falls into the range of 27–33 MPa. As for the $Zn(MeIm)_2$ herein synthesized using the reaction–diffusion method, the P_{in} is around 30 MPa, which is consistent with the result reported by Patarin et al. [27]. In addition, $P–\Delta V$ diagram shows a weak hysteresis as the pressure is unloaded. From the energy perspective, the spontaneous outflow of the intruded water is facilitated by the hydrophobic nature of the nanopores, resulting in the lower extrusion pressure (P_{ext}) than the corresponding P_{in} for each system [64]. As for the bimetallic sample-involved systems, intrusion volume (V_{in}) is significantly enlarged due to the increase in the pore volume of the frameworks with Co doping. All systems exhibit smaller extrusion volume (V_{ext}) than V_{in}, suggesting that the confined water cannot be withdrawn completely as the pressure is unloaded. In the case of the $Co_{0.5}Zn_{0.5}$-$(MeIm)_2$ sample having comparative contents of Co and Zn, the intrusion–extrusion curve has the minimal hysteresis while the V_{ext} (0.40 $mL·g^{-1}$) is the closest to the corresponding V_{in} (0.41 $mL·g^{-1}$). Furthermore, both higher P_{in} and larger V_{in} can lead to higher energy capacity [65]. The quasi-static mechanical measurements indicate the transition of system from shock-absorber to molecular spring as the Co doping percentage increases from 10% to 50%. However, the energy conversions of these systems are all lower as compared to a standard shock-absorber or molecular spring. Once the ZIF structure reaches complete replacement with Co, the system changes into a shock-absorber again. In terms of energy conversion, the $Co_{0.5}Zn_{0.5}$-$(MeIm)_2$ sample, giving an efficiency of 78%, exhibits the best performance among all these Co_xZn_{1-x}-$(MeIm)_2$ samples. As a

Table 1   Pore structure analyses of Co_xZn_{1-x}-$(MeIm)_2$[a]

Sample	S_{BET} (m²·g⁻¹)	$V_{Micro-HK}$ (cm³·g⁻¹)	$V_{Meso-BJH}$ (cm³·g⁻¹)	$W_{Micro-HK}$ (nm)	$W_{Avg-BET}$ (nm)
$Zn(MeIm)_2$	1550	0.51	0.04	1.09, 1.19, 1.30–1.35	1.51
$Co_{0.1}Zn_{0.9}$-$(MeIm)_2$	1840	0.61	0.07	1.09, 1.19, 1.30–1.35	1.54
$Co_{0.3}Zn_{0.7}$-$(MeIm)_2$	1637	0.56	0.04	1.09, 1.19, 1.30–1.35	1.48
$Co_{0.5}Zn_{0.5}$-$(MeIm)_2$	1636	0.56	0.10	1.09, 1.19, 1.30–1.35	1.61
$Co_{0.7}Zn_{0.3}$-$(MeIm)_2$	1690	0.57	0.08	1.09, 1.30–1.35	1.56
$Co(MeIm)_2$	1201	0.52	0.05	1.19	1.93

[a]S_{BET}: specific surface area calculated by BET method; $V_{Micro-HK}$: micropore volume calculated by HK method; $V_{Meso-HK}$: mesopore volume calculated by BJH method; $W_{Micro-HK}$: sizes of main micropores; and $W_{Avg-BET}$: average pore size.

Table 2   Geometric properties of the Co_xZn_{1-x}-$(MeIm)_2$ models computed using Zeo++[a]

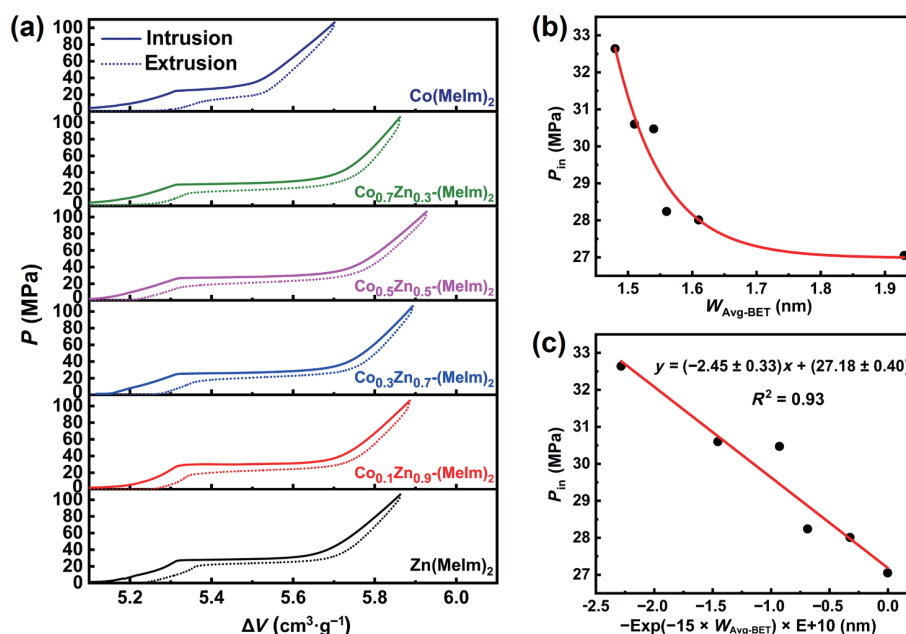| Model structure	S_{AC} (m²·g⁻¹)	V_{PO} (cm³·g⁻¹)	W (nm)
$Zn(MeIm)_2$	1433	0.463	1.11, 1.14
$Co_{0.1}Zn_{0.9}$-$(MeIm)_2$	1496	0.474	1.09, 1.12
$Co_{0.3}Zn_{0.7}$-$(MeIm)_2$	1490	0.470	1.08, 1.11
$Co_{0.5}Zn_{0.5}$-$(MeIm)_2$	1516	0.472	1.08, 1.12
$Co_{0.7}Zn_{0.3}$-$(MeIm)_2$	1559	0.474	1.08, 1.11
$Co(MeIm)_2$	1600	0.423	1.01, 1.05

[a]W: most probable pore size.

Figure 2   (a) Pressure versus intrusion volume curves of different {Co_xZn_{1-x}-$(MeIm)_2$+water} systems. (b) Relationship between the average pore size and the intrusion pressure. (c) Fitted linear relationship for P_{in} versus $-Exp(-15 \times W_{Avg-BET}) \times E+10$.

result, the $Co_{0.5}Zn_{0.5}$-$(MeIm)_2$ structure can be expected to endow the HLS system with promising performance required by a molecular spring. Meanwhile, it is worth noting that the intrusion volume of water is always smaller than the pore volume of the material itself. It can be explained by the fact that the density of confined water is lower than that of the bulk water. According to the result reported by Desbines et al., the density of water confined in the nanopores of silicalite-1 was only 0.6 g·mL⁻¹ [66]. To reveal the relationship between the intrusion pressure and pore size, we correlate the average pore sizes with the intrusion pressures and present the fitting results in Fig. 2(b). Overall, the intrusion pressure decreases with increasing pore size. Furthermore, we linearize the correlation data in Fig. 2(c), in which the linear relationship implies that the intrusion pressure can be precisely controlled via tuning the pore size through simply adjusting the

Co to Zn ratio during the sample synthesis. Moreover, we used CO_2 as a probing gas to determine the micropore size distribution of the samples, further confirming the correlation between pore size and P_{in} (see Figs. S9 and S10 and Table S6 in the ESM).

Moreover, we performed XRD analysis on the samples recycled from the intrusion–extrusion experiment to examine their structural changes. From the XRD patterns in Fig. S3(b) in the ESM, an additional peak at $2\theta = 11.2°$ can be recognized. In order to verify the factors relating to the structural change during intrusion–extrusion tests, two sets of samples were prepared for XRD analysis. One set of Co_xZn_{1-x}-$(MeIm)_2$ samples was immersed in water at room temperature for one week (Fig. S3(c) in the ESM) and another set of samples was obtained via performing the tests on corresponding Co_xZn_{1-x}-$(MeIm)_2$ samples without water involvement (Fig. S3(d) in the ESM). The XRD

**Table 3** Characteristic parameters for different {Co$_x$Zn$_{1-x}$-(MeIm)$_2$+water} systems[a]

System	P_{in} (Mpa)	P_{ext} (Mpa)	V_{in} (mL·g^{-1})	V_{ext} (mL·g^{-1})	E_{in} (J·g^{-1})	E_{ext} (J·g^{-1})	Y_e	Behavior
Zn(MeIm)$_2$	30.60	24.76	0.37	0.32	11.60	8.01	0.69	SA
Co$_{0.1}$Zn$_{0.9}$-(MeIm)$_2$	30.47	23.65	0.43	0.40	13.94	9.76	0.70	SA
Co$_{0.3}$Zn$_{0.7}$-(MeIm)$_2$	32.64	22.42	0.41	0.38	14.11	8.93	0.63	SA
Co$_{0.5}$Zn$_{0.5}$-(MeIm)$_2$	28.01	21.48	0.41	0.40	11.35	8.88	0.78	S
Co$_{0.7}$Zn$_{0.3}$-(MeIm)$_2$	28.24	20.86	0.41	0.38	11.44	7.97	0.70	SA
Co(MeIm)$_2$	27.05	16.41	0.22	0.17	6.38	2.76	0.43	SA

[a]E_{in}: stored energy; E_{ext}: released energy; Y_e: energy yield. Values of the P_{in} and P_{ext} correspond to that of the half volume total variation [67]. And the V_{in} and V_{ext} depend on the length of the corresponding pressure plateau. E_{in} and E_{ext} are given by $E = \int_{V_0}^{V_f} P dV$, where V_0 is the initial volume and V_f is the final volume. Y_e is given by E_{ext}/E_{in}. SA and S represent the shock-absorber and spring, respectively.

results suggest that the pressure loading has no effect on their crystalline structures, whereas the presence of water causes an additional XRD peak. During a normal intrusion–extrusion experiment, the water confined in the cage exists in the form of hydrogen bonded multimers. After one intrusion–extrusion cycle, we subjected the material to heating treatment at 180 and 240 °C (see Figs. S3(e) and S3(f) in the ESM), respectively. Consequently, the additional peak of $2\theta = 11.2°$ disappears. According to the XRD confirmation, it can be concluded that the structural change can be attributed to the presence of water. Present findings differ from the results of the {Zn(MeIm)$_2$+water} system previously reported by Ortiz et al [68]. The FTIR characterization on all post-intrusion samples indicates the structural changes in the Co(MeIm)$_2$ sample, while other samples keep their original structure during water intrusion (see Fig. S11 in the ESM). In addition, all samples remain high hydrophobicity after liquid water intrusion (see Fig. S12 in the ESM). In order to further evaluate the stability of these Co$_x$Zn$_{1-x}$-(MeIm)$_2$ samples having exposure to liquid water, we conducted 30 successive intrusion–extrusion tests on the same sample of Co$_{0.5}$Zn$_{0.5}$-(MeIm)$_2$. From Fig. 3, all cycles give almost overlapped intrusion–extrusion curves with slight shifts (no more than 1 MPa) of the intrusion–extrusion pressures (see Table S7 in the ESM). The observed slight pressure variation can be ascribed to the expansion of the framework volume induced by the intrusion of liquid water, which agrees well with previous reports [31]. The XRD patterns of Co$_{0.5}$Zn$_{0.5}$-(MeIm)$_2$ after undergoing different test cycles were recorded in Fig. S13 in the ESM. All recycled samples show very consistent characteristic peaks with the fresh Co$_{0.5}$Zn$_{0.5}$-(MeIm)$_2$ sample, suggesting the high stability of the heterometallic ZIF structures and the fully reversible structure transformation induced by the water intrusion.

Furthermore, molecular dynamics simulations were performed to understand the underlying intermolecular interaction mechanism of water as intruding into the nanoporous materials of bimetallic ZIFs. RDF was used to analyze the association structure of water confined in all the frameworks upon pressure-induced intrusion–extrusion of water. RDFs for O–O, O–H, and H–H of bulk and confined water were calculated at different pressures (see Fig. S14 in the ESM). From the simulation results, as compared to the monometallic Zn(MeIm)$_2$, the RDFs of Co-doped structures have much lower peak intensities, corresponding to the largely reduced appearance frequency of water molecules. It can be explained that the Co-doping leads to higher specific surface area and pore volume, which endows the confined water molecules with larger space and, therefore, results in lower density distribution. In addition, all peaks in the RDF curves of different structures show almost the same positions, indicating that water molecules intrude into the Co/Zn ZIFs in the same form. The RDFs of atom pairs among water molecules at 30 MPa are shown
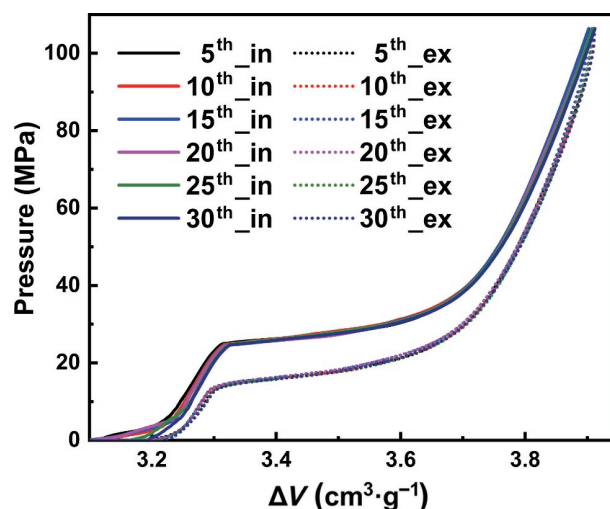
Figure 3 The repeated intrusion–extrusion curves for 30 consecutive cycles.

in Fig. 4. In Fig. 4(a) of the bulk water, the $g_{O-O}(r)$ pattern shows the first peak at r of 2.72 Å, which represents the first-shell layer of water cluster, indicating the O–O distance between water molecules with the highest probability of occurrence. The peaks located at 4.5 Å are assigned to the second-shell layer of water cluster. Our findings are in agreement with the calculation results reported by Sharma et al. [69].

In the $g_{O-H}(r)$ pattern, there are three peaks located at 0.99, 1.78, and 3.25 Å. The first peak of 0.99 Å corresponds to the bond length of O–H. 1.78 Å represents the most likely length of the hydrogen bond between the donor H in one water molecule and the acceptor O in another one. The first valley of $g_{O-H}(r)$ is located at 2.4 Å, which indicates the maximum distance to form the intermolecular O–H hydrogen bond. 3.25 Å represents the distance between the O and H atoms without forming hydrogen bond. The distribution of $g_{H-H}(r)$ largely depends on the situations of both $g_{O-H}(r)$ and $g_{O-O}(r)$. The $g_{H-H}(r)$ peaks are located at 1.49 and 2.44 Å, representing the distances between the intramolecular and intermolecular hydrogen atoms, respectively. As for the {Co$_x$Zn$_{1-x}$-(MeIm)$_2$+water} systems, using the intrusion volume obtained from the intrusion–extrusion experiments, we evaluated the number of water molecules confined in each unit cell of different frameworks (see Table S8 in the ESM). RDFs of water in both states of the pre-intrusion and post-intrusion were analyzed in order to understand the evolution of associative structures of water multimers along with the intrusion into the nanopores of ZIFs. From Figs. 4(c), 4(e), and 4(g), the RDF peaks relating to the first-shell layer shift to larger distances of 3.33 Å for O–O, 2.56 Å for O–H, and 3.22 Å for H–H. As for the second-shell layer, their corresponding peaks move to 6.14 Å for O–O and 3.85 Å for O–H. The calculated distributions of $g_{O-H}(r)$, $g_{O-O}(r)$, and $g_{H-H}(r)$
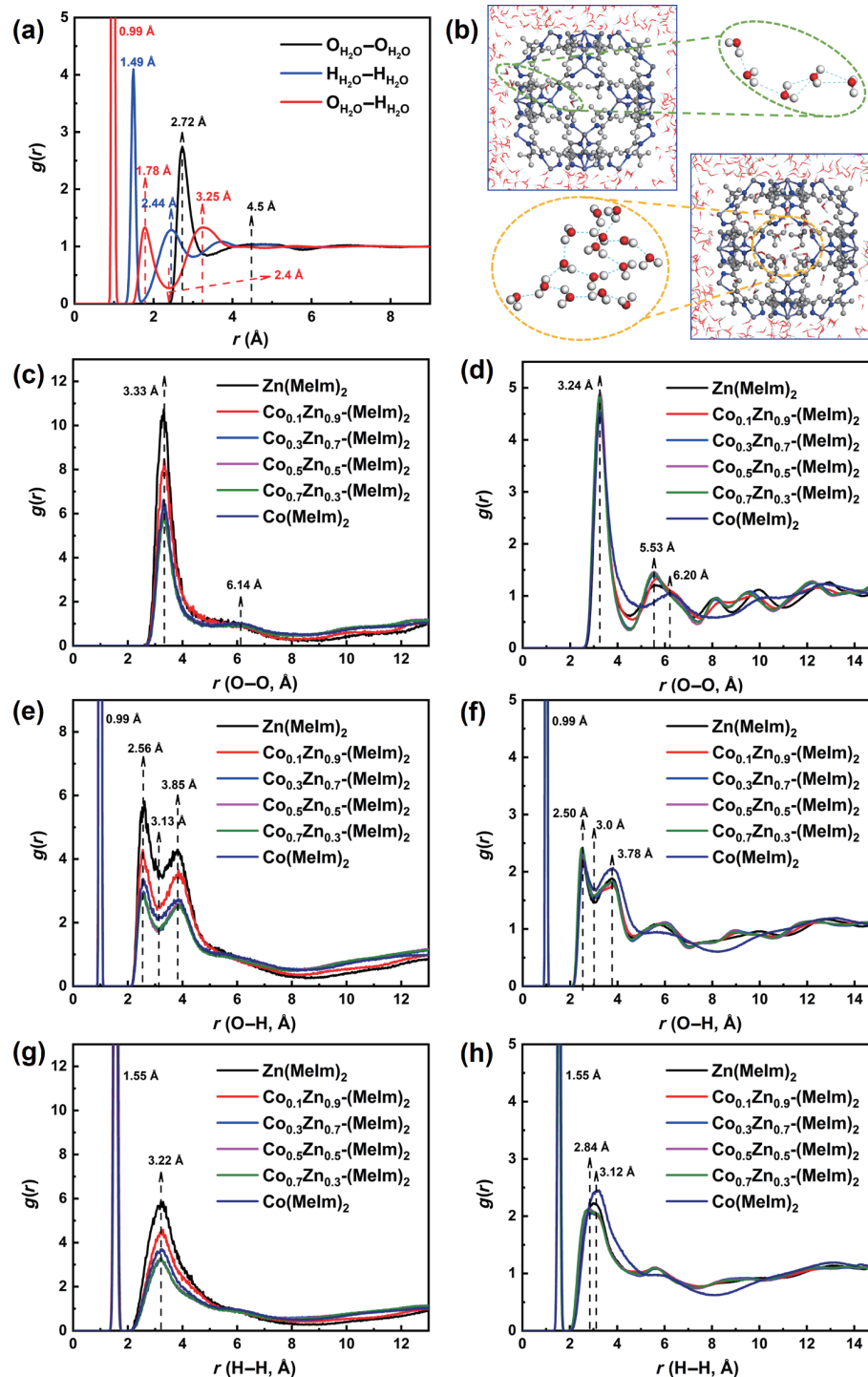
Figure 4 RDFs of atom pairs among water molecules at 30 MPa. (a) Bulk water. (b) Diagrams for the pre-intrusion and post-intrusion of water multimer in the structural model of $Co_{0.5}Zn_{0.5}$-(MeIm)$_2$. Pre-intrusion situation for (c) g_{O-O}, (e) g_{O-H}, and (g) g_{H-H}, and post-intrusion situation for (d) g_{O-O}, (f) g_{O-H}, and (h) g_{H-H} of water in Co_xZn_{1-x}-(MeIm)$_2$ (x = 0, 0.1, 0.3, 0.5, 0.7, and 1).

indicate that the intermolecular distances within all these intrusion systems are significantly larger than those of bulk water. The maximum distance of hydrogen bond formation also ranges from 2.4 Å in bulk water to 3.13 Å in confined water. Furthermore, the $g_{O-O}(r)$ intensity ratio of the first peak to the second one is found to increase from 2.75 for the bulk water to 5.74–10.72 in the pre-intrusion state. Both increased intermolecular distance and peak intensity ratio suggest the significant impact of the confinement on the first and second-shell layers of the associative water multimers [70] and the dissociation effect of the hydrogen bond during the intrusion of water molecules [71]. Once intrusion happens, the water species are confined in more compact spaces of frameworks and therefore show slightly reduced interatomic

distances (the first shell layers: 3.24 Å for O–O, 2.50 Å for O–H, and 2.84 and 3.12 Å for H–H. The second shell layers: 5.53 and 6.20 Å for O–O, and 3.78 Å for O–H) (see Figs. 4(d), 4(f), and 4(h)).

The dissociation of the HB structure is further confirmed through the statistical analysis. The calculated average numbers of HBs related to each water molecule at different pressures, N_{HB}, are listed in Table S9 in the ESM. In a bulk water box, N_{HB} is observed to be of ~ 4. The present result is in good agreement with the previous findings that the bulk water has a local structure of tetrahedral HB network [72]. In addition, N_{HB} rises slightly with an increasing pressure. In all cases of pre-intrusion state, N_{HB} has lower values, ranging from 1.6 to 3.0. Also, it shows a decreasing

trend in response to the increase in pressure, which agrees well with the results reported by Xie et al. [47]. In addition, the statistical percentage of water molecules forming 0–6 HBs at different pressures in every framework is presented in Fig. S15 in the ESM. From the calculation results, the water molecules forming 2–3 HBs account for the largest proportion. Furthermore, snapshots of water molecule arrangement corresponding to the pre-intrusion state in different structures of Co_xZn_{1-x}-(MeIm)$_2$ at 30 MPa are obtained through performing the MD simulation. From the molecule structures illustrated in Fig. 5, all these water multimers in different frameworks under pressure have approximately linear structures. As for the post-intrusion situation, the associative configurations of water confined in nanopores of these frameworks transition from linear to tetrahedral structure, however does not completely return to the associative state of the bulk water. The N_{HB} finds the values ranging from 3 to 4 (see Table S9 in the ESM), which are greater than those of the pre-intrusion situation. Especially, the N_{HB} of the $Co(MeIm)_2$-involved system is less than 2. It can be ascribed to the strong cationic association of Co (exhibiting greater hydrophilicity than Zn structure). The cationic interactions weaken the hydrogen bonding among water molecules and therefore reduce the number of HBs. The same results have been found by Calero et al., [73] as they performed a simulation investigation on the effect of cations on H-bonding of water in zeolites. It was concluded that the hydrogen bonding of water molecules can be largely weakened in the cationic zeolites. The average number of HBs in confined water was found to be about 2 in hydrophilic LTA zeolites and it is smaller than that in a hydrophobic pure silica structure of ITQ-29. Based on the analyses of RDFs and hydrogen bond, for the first time, we present that the water multimers intrude into the nanopores of ZIFs in the chain-like forms upon the pressure-induced dissociation of hydrogen bonds.

4 Conclusions

We synthesized a series of heterometallic ZIFs with tunable pore sizes via regulating the Co to Zn molar ratios in order to investigate the intrusion–extrusion of liquid water in confined nanopores. The quasi-static mechanical measurements reveal the negative correlation between the intrusion pressure and the nanopore size. The $Co_{0.5}Zn_{0.5}$-(MeIm)$_2$ sample is of the highest energy conversion efficiency of 78% and can be expected to endow the HLS system with desired performance required by a molecular spring. 30 cycling tests confirm the reversible structure change of Co/Zn bimetallic ZIFs encountering pressure-induced water intrusion. MD simulations reveal that the water multimers intrude into the nanopores of ZIFs in the chain-like forms upon the pressure-induced dissociation of hydrogen bonds. Water molecules in the pre-intrusion state exhibit the reducing HBs in response to the increase of pressure and the linear structure with average HB number of 1.6–3.0. After transition to the post-intrusion situation, the associative configuration of water changes to the tetrahedral structure. The present work provides an approach to understanding the intrusion–extrusion mechanism of the liquid medium in the confined nanopores and feasible strategy for the rational design and development of functional guest–host systems based on porous architectures.

Electronic Supplementary Material: Supplementary material (experimental setup, SEM, EDS, pore structure analysis results, ICP-OES experimental results of Co_xZn_{1-x}-(MeIm)$_2$, XRD results before and after intrusion, experimental and simulated water vapor adsorption results, cell parameters, mechanical properties data of cyclic intrusion–extrusion, charge calculation results, force field parameters of SPC model of water molecules, theoretical pore size distribution calculation results, RDF calculation results of water molecules in the cell at different pressures, and statistics of the average number of hydrogen bonds formed per water molecule) is available in the online version of this article at https://doi.org/10.1007/s12274-023-5967-5.
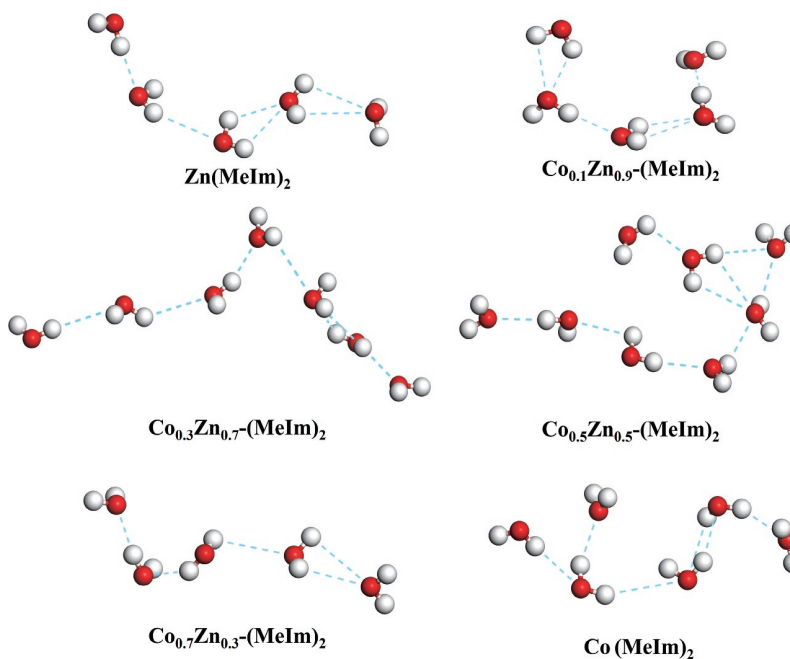

Figure 5 Snapshots of water molecule arrangement in different structures of Co_xZn_{1-x}-(MeIm)$_2$ at 30 MPa.

References

[1] Goeminne, R.; Krause, S.; Kaskel, S.; Verstraelen, T.; Evans, J. D. Charting the complete thermodynamic landscape of gas adsorption for a responsive metal-organic framework. *J. Am. Chem. Soc.* **2021**, *143*, 4143–4147.

[2] Yang, Y. B.; Yang, X. D.; Liang, L.; Gao, Y. Y.; Cheng, H. Y.; Li, X. M.; Zou, M. C.; Ma, R. Z.; Yuan, Q. Duan, X. F. Large-area graphene-nanomesh/carbon-nanotube hybrid membranes for ionic and molecular nanofiltration. *Science* **2019**, *364*, 1057–1062.

[3] Fang, W.; Wang, C. T.; Liu, Z. Q.; Wang, L.; Liu, L.; Li, H. J.; Xu, S. D.; Zheng, A. M.; Qin, X. D.; Liu, L. J. et al. Physical mixing of a catalyst and a hydrophobic polymer promotes CO hydrogenation through dehydration. *Science* **2022**, *377*, 406–410.

[4] Zhang, W. Y.; Wei, S.; Wu, Y. N.; Wang, Y. L.; Zhang, M.; Roy, D.; Wang, H.; Yuan, J. Y.; Zhao, Q. Poly(ionic liquid)-derived graphitic nanoporous carbon membrane enables superior supercapacitive energy storage. *ACS Nano* **2019**, *13*, 10261–10271.

[5] Lee, A.; Hudson, A. R.; Shiwarski, D. J.; Tashman, J. W.; Hinton, T. J.; Yerneni, S.; Bliley, J. M.; Campbell, P. G.; Feinberg, A. W. 3D bioprinting of collagen to rebuild components of the human heart. *Science* **2019**, *365*, 482–487.

[6] El-Kady, M. F.; Strong, V.; Dubin, S.; Kaner, R. B. Laser scribing of high-performance and flexible graphene-based electrochemical capacitors. *Science* **2012**, *335*, 1326–1330.

[7] Eroshenko, V.; Regis, R. C.; Soulard, M.; Patarin, J. Energetics: A new field of applications for hydrophobic zeolites. *J. Am. Chem. Soc.* **2001**, *123*, 8129–8130.

[8] Yu, M. C.; Chen, Q.; Gao, X. Theoretical and experimental investigation of molecular spring isolator. *Microsyst. Technol.* **2017**, *23*, 285–292.

[9] Zhou, X.; Miao, Y. R.; Shaw, W. L.; Suslick, K. S.; Dlott, D. D. Shock wave energy absorption in metal-organic framework. *J. Am. Chem. Soc.* **2019**, *141*, 2220–2223.

[10] Tinti, A.; Giacomello, A.; Grosu, Y.; Casciola, C. M. Intrusion and extrusion of water in hydrophobic nanopores. *Proc. Natl. Acad. Sci. USA* **2017**, *114*, E10266–E10273.

[11] Fraux, G.; Coudert, F. X.; Boutin, A.; Fuchs, A. H. Forced intrusion of water and aqueous solutions in microporous materials: From fundamental thermodynamics to energy storage devices. *Chem. Soc. Rev.* **2017**, *46*, 7421–7437.

[12] Liu, L.; Chen, X.; Lu, W. Y.; Han, A. J.; Qiao, Y. Infiltration of electrolytes in molecular-sized nanopores. *Phys. Rev. Lett.* **2009**, *102*, 184501.

[13] Zhao, J. B.; Culligan, P. J.; Germaine, J. T.; Chen, X. Experimental study on energy dissipation of electrolytes in nanopores. *Langmuir* **2009**, *25*, 12687–12696.

[14] Pillot, M.; Lebeau, B.; Nouali, H.; Daou, T. J.; Patarin, J.; Ryzhikov, A. High pressure intrusion of water and LiCl aqueous solutions in hydrophobic KIT-6 mesoporous silica: Influence of the grafted group nature. *Micropor. Mesopor. Mater.* **2019**, *280*, 248–255.

[15] Huve, J.; Daou, T. J.; Nouali, H.; Patarin, J.; Ryzhikov, A. The effect of nanostructures on high pressure intrusion-extrusion of water and electrolyte solutions in hierarchical nanoboxes of silicalite-1. *New J. Chem.* **2020**, *44*, 273–281.

[16] Isaac, C.; Confalonieri, G.; Nouali, H.; Paillaud, J. L.; Arletti, R.; Daou, T. J.; Ryzhikov, A. Unusual high-pressure intrusion-extrusion behavior of electrolyte solutions in Mu-26, a pure silica zeolite of topology STF. *Micropor. Mesopor. Mater.* **2020**, *298*, 110047.

[17] Trzpit, M.; Soulard, M.; Patarin, J. The pure silica Chabazite: A high volume molecular spring at low pressure for energy storage. *Chem. Lett.* **2007**, *36*, 980–981.

[18] Qiao, Y.; Punyamurtula, V. K.; Xian, G. J.; Karbhari, V. M.; Han, A. J. Conversion of mechanical work to interfacial tension in a nanoporous silica gel. *Appl. Phys. Lett.* **2008**, *92*, 063109.

[19] Chen, X.; Surani, F. B.; Kong, X. G.; Punyamurtula, V. K.; Qiao, Y. Energy absorption performance of steel tubes enhanced by a nanoporous material functionalized liquid. *Appl. Phys. Lett.* **2006**, *89*, 241918.

[20] Trzpit, M.; Rigolet, S.; Paillaud, J. L.; Marichal, C.; Soulard, M.; Patarin, J. Pure silica Chabazite molecular spring: A structural study on water intrusion-extrusion processes. *J. Phys. Chem. B* **2008**, *112*, 7257–7266.

[21] Tzanis, L.; Trzpit, M.; Soulard, M.; Patarin, J. Energetic performances of channel and cage-type zeosils. *J. Phys. Chem. C* **2012**, *116*, 20389–20395.

[22] Tzanis, L.; Trzpit, M.; Soulard, M.; Patarin, J. High pressure water intrusion investigation of pure silica 1D channel AFI, MTW and TON-type zeolites. *Micropor. Mesopor. Mater.* **2011**, *146*, 119–126.

[23] Khay, I.; Tzanis, L.; Daou, T. J.; Nouali, H.; Ryzhikov, A.; Patarin, J. Energetic behavior of the pure silica ITQ-12 (ITW) zeolite under high pressure water intrusion. *Phys. Chem. Chem. Phys.* **2013**, *15*, 20320–20325.

[24] Grosu, Y.; Li, M.; Peng, Y. L.; Luo, D.; Li, D.; Faik, A.; Nedelec, J. M.; Grolier, J. P. A highly stable nonhysteretic {Cu₂(tebpz) MOF+water} molecular spring. *ChemPhysChem* **2016**, *17*, 3359–3364.

[25] Park, K. S.; Ni, Z.; Côté, A. P.; Choi, J. Y.; Huang, R. D.; Uribe-Romo, F. J.; Chae, H. K.; O'Keeffe, M.; Yaghi, O. M. Exceptional chemical and thermal stability of zeolitic imidazolate frameworks. *Proc. Natl. Acad. Sci. USA* **2006**, *103*, 10186–10191.

[26] Banerjee, R.; Phan, A.; Wang, B.; Knobler, C.; Furukawa, H.; O'Keeffe, M.; Yaghi, O. M. High-throughput synthesis of zeolitic imidazolate frameworks and application to CO₂ capture. *Science* **2008**, *319*, 939–943.

[27] Ortiz, G.; Nouali, H.; Marichal, C.; Chaplais, G.; Patarin, J. Energetic performances of the metal-organic framework ZIF-8 obtained using high pressure water intrusion-extrusion experiments. *Phys. Chem. Chem. Phys.* **2013**, *15*, 4888–4891.

[28] Sun, Y. T.; Li, Y. B.; Tan, J. C. Framework flexibility of ZIF-8 under liquid intrusion: Discovering time-dependent mechanical response and structural relaxation. *Phys. Chem. Chem. Phys.* **2018**, *20*, 10108–10113.

[29] Hu, Y.; Kazemian, H.; Rohani, S.; Huang, Y. N.; Song, Y. *In situ* high pressure study of ZIF-8 by FTIR spectroscopy. *Chem. Commun.* **2011**, *47*, 12694–12696.

[30] Chen, S. L.; Li, X.; Dong, E. L.; Lv, H.; Yang, X. B.; Liu, R.; Liu, B. B. Intrinsic and extrinsic responses of ZIF-8 under high pressure: A combined Raman and X-ray diffraction investigation. *J. Phys. Chem. C* **2019**, *123*, 29693–29707.

[31] Tortora, M.; Zajdel, P.; Lowe, A. R.; Chorążewski, M.; Leão, J. B.; Jensen, G. V.; Bleuel, M.; Giacomello, A.; Casciola, C. M.; Meloni, S. et al. Giant negative compressibility by liquid intrusion into superhydrophobic flexible nanoporous frameworks. *Nano Lett.* **2021**, *21*, 2848–2853.

[32] Zajdel, P.; Madden, D. G.; Babu, R.; Tortora, M.; Mirani, D.; Tsyrin, N. N.; Bartolomé, L.; Amayuelas, E.; Fairen-Jimenez, D.; Lowe, A. R. et al. Turning molecular springs into Nano-shock absorbers: The effect of macroscopic morphology and crystal size on the dynamic hysteresis of water intrusion-extrusion into-from hydrophobic nanopores. *ACS Appl. Mater. Interfaces* **2022**, *14*, 26699–26713.

[33] Sun, Y. T.; Rogge, S. M. J.; Lamaire, A.; Vandenbrande, S.; Wieme, J.; Siviour, C. R.; Van Speybroeck, V.; Tan, J. C. High-rate nanofluidic energy absorption in porous zeolitic frameworks. *Nat. Mater.* **2021**, *20*, 1015–1023.

[34] Borjigin, T.; Sun, F. X.; Zhang, J. L.; Cai, K.; Ren, H.; Zhu, G. S. A microporous metal-organic framework with high stability for GC separation of alcohols from water. *Chem. Commun.* **2012**, *48*, 7613–7615.

[35] Sun, Y. T.; Li, Y. B.; Tan, J. C. Liquid intrusion into zeolitic imidazolate framework-7 nanocrystals: Exposing the roles of phase transition and gate opening to enable energy absorption applications. *ACS Appl. Mater. Interfaces* **2018**, *10*, 41831–41838.

[36] Chakraborty, S.; Kumar, H.; Dasgupta, C.; Maiti, P. K. Confined water: Structure, dynamics, and thermodynamics. *Acc. Chem. Res.* **2017**, *50*, 2139–2146.

[37] Zhou, T. C.; Bai, P.; Siepmann, J. I.; Clark, A. E. Deconstructing the confinement effect upon the organization and dynamics of water in hydrophobic nanoporous materials: Lessons learned from zeolites. *J. Phys. Chem. C* **2017**, *121*, 22015–22024.

[38] Paulo, G.; Gubbiotti, A.; Grosu, Y.; Meloni, S.; Giacomello, A. The

impact of secondary channels on the wetting properties of interconnected hydrophobic nanopores. *Commun. Phys.* **2023**, *6*, 21.

[39] Bushuev, Y. G.; Grosu, Y.; Chorążewski, M. A.; Meloni, S. Subnanometer topological tuning of the liquid intrusion/extrusion characteristics of hydrophobic micropores. *Nano Lett.* **2022**, *22*, 2164–2169.

[40] Saliba, D.; Ammar, M.; Rammal, M.; Al-Ghoul, M.; Hmadeh, M. Crystal growth of ZIF-8, ZIF-67, and their mixed-metal derivatives. *J. Am. Chem. Soc.* **2018**, *140*, 1812–1823.

[41] Cai, H. D.; Zhang, L. L.; Xu, J. S.; Huang, J. H.; Wei, X. L.; Wang, L.; Song, Z. Y.; Long, W. Cobalt-free $La_{0.5}Sr_{0.5}Fe_{0.9}Mo_{0.1}O_{3-\delta}$ electrode for symmetrical SOFC running on H_2 and CO fuels. *Electrochim. Acta.* **2019**, *320*, 134642.

[42] Xu, X. L.; Zhang, X. M.; Xia, Z. X.; Sun, R. L.; Li, H. Q.; Wang, J. H.; Yu, S. S.; Wang, S. L.; Sun, G. Q. Solid phase microwave-assisted fabrication of Fe-doped ZIF-8 for single-atom Fe-N-C electrocatalysts on oxygen reduction. *J. Energy Chem.* **2021**, *54*, 579–586.

[43] Benzaqui, M.; Semino, R.; Menguy, N.; Carn, F.; Kundu, T.; Guigner, J. M.; McKeown, N. B.; Msayib, K. J.; Carta, M.; Malpass-Evans, R. et al. Toward an understanding of the microstructure and interfacial properties of PIMs/ZIF-8 mixed matrix membranes. *ACS Appl. Mater. Interfaces* **2016**, *8*, 27311–27321.

[44] Gao, M. Z.; Wang, J.; Rong, Z. H.; Shi, Q.; Dong, J. X. A combined experimental-computational investigation on water adsorption in various ZIFs with the SOD and RHO topologies. *RSC Adv.* **2018**, *8*, 39627–39634.

[45] Skarmoutsos, I.; Eddaoudi, M.; Maurin, G. Highly efficient rare-earth-based metal-organic frameworks for water adsorption: A molecular modeling approach. *J. Phys. Chem. C* **2019**, *123*, 26989–26999.

[46] Zhang, H.; Singer, S. J. Analysis of the subcritical carbon dioxide-water interface. *J. Phys. Chem. A* **2011**, *115*, 6285–6296.

[47] Tang, Y. B.; Xie, S. J. Structure and dynamics of a water/methanol mixture confined in zeolitic imidazolate framework ZIF-8 from atomistic simulations. *Phys. Chem. Chem. Phys.* **2022**, *24*, 5220–5232.

[48] Li, Z.; Zeng, H. C. Surface and bulk integrations of single-layered Au or Ag nanoparticles onto designated crystal planes {110} or {100} of ZIF-8. *Chem. Mater.* **2013**, *25*, 1761–1768.

[49] Wang, M.; Liu, J. X.; Guo, C. M.; Gao, X. S.; Gong, C. H.; Wang, Y.; Liu, B.; Li, X. X.; Gurzadyan, G. G.; Sun, L. C. Metal-organic frameworks (ZIF-67) as efficient cocatalysts for photocatalytic reduction of CO_2: The role of the morphology effect. *J. Mater. Chem. A* **2018**, *6*, 4768–4775.

[50] Cravillon, J.; Nayuk, R.; Springer, S.; Feldhoff, A.; Huber, K.; Wiebcke, M. Controlling zeolitic imidazolate framework nano- and microcrystal formation: Insight into crystal growth by time-resolved *in situ* static light scattering. *Chem. Mater.* **2011**, *23*, 2130–2141.

[51] Shen, K.; Zhang, L.; Chen, X. D.; Liu, L. M.; Zhang, D. L.; Han, Y.; Chen, J. Y.; Long, J. L.; Luque, R.; Li, Y. W. et al. Ordered macro-microporous metal-organic framework single crystals. *Science* **2018**, *359*, 206–210.

[52] James, J. B.; Lin, Y. S. Kinetics of ZIF-8 Thermal decomposition in inert, oxidizing, and reducing environments. *J. Phys. Chem. C* **2016**, *120*, 14015–14026.

[53] Zhu, R. M.; Ding, J. W.; Yang, J. P.; Pang, H.; Xu, Q.; Zhang, D. L.; Braunstein, P. Quasi-ZIF-67 for boosted oxygen evolution reaction catalytic activity via a low temperature calcination. *ACS Appl. Mater. Interfaces* **2020**, *12*, 25037–25041.

[54] Zhao, Y. L.; Wei, Y. Y.; Lyu, L.; Hou, Q. Q.; Caro, J.; Wang, H. H. Flexible polypropylene-supported ZIF-8 membranes for highly efficient propene/propane separation. *J. Am. Chem. Soc.* **2020**, *142*, 20915–20919.

[55] Mor, J.; Sharma, S. K.; Utpalla, P.; Bahadur, J.; Prakash, J.; Kumar, A.; Pujari, P. K. Pore architecture evolution and OER catalytic activity of hollow Co/Zn zeolitic imidazolate frameworks. *Micropor. Mesopor. Mater.* **2022**, *335*, 111814.

[56] Ordoñez, M. J. C.; Balkus, K. J.; Ferraris, J. P.; Musselman, I. H. Molecular sieving realized with ZIF-8/matrimid® mixed-matrix membranes. *J. Membr. Sci.* **2010**, *361*, 28–37.

[57] Tanaka, S.; Tanaka, Y. A simple step toward enhancing hydrothermal stability of ZIF-8. *ACS Omega* **2019**, *4*, 19905–19912.

[58] Wu, C. H.; Xie, D. G.; Mei, Y. J.; Xiu, Z. F.; Poduska, K. M.; Li, D. C.; Xu, B.; Sun, D. F. Unveiling the thermolysis natures of ZIF-8 and ZIF-67 by employing *in situ* structural characterization studies. *Phys. Chem. Chem. Phys.* **2019**, *21*, 17571–17577.

[59] Willems, T. F.; Rycroft, C. H.; Kazi, M.; Meza, J. C.; Haranczyk, M. Algorithms and tools for high-throughput geometry-based analysis of crystalline porous materials. *Micropor. Mesopor. Mater.* **2012**, *149*, 134–141.

[60] Calero, S.; Gómez-Álvarez, P. Underlying adsorption mechanisms of water in hydrophobic and hydrophilic zeolite imidazolate frameworks: ZIF-71 and ZIF-90. *J. Phys. Chem. C* **2015**, *119*, 23774–23780.

[61] Jayachandrababu, K. C.; Sholl, D. S.; Nair, S. Structural and mechanistic differences in mixed-linker zeolitic imidazolate framework synthesis by solvent assisted linker exchange and *de novo* routes. *J. Am. Chem. Soc.* **2017**, *139*, 5906–5915.

[62] Krishna, R.; Van Baten, J. M. Water/alcohol mixture adsorption in hydrophobic materials: Enhanced water ingress caused by hydrogen bonding. *ACS Omega* **2020**, *5*, 28393–28402.

[63] Mortada, B.; Chaplais, G.; Nouali, H.; Marichal, C.; Patarin, J. Phase transformations of metal-organic frameworks MAF-6 and ZIF-71 during intrusion-extrusion experiments. *J. Phys. Chem. C* **2019**, *123*, 4319–4328.

[64] Gao, Y.; Li, M. Z.; Zhang, Y.; Lu, W. Y.; Xu, B. X. Spontaneous outflow efficiency of confined liquid in hydrophobic nanopores. *Proc. Natl. Acad. Sci. USA* **2020**, *117*, 25246–25253.

[65] Mortada, B.; Chaplais, G.; Veremeienko, V.; Nouali, H.; Marichal, C.; Patarin, J. Energetic performances of ZIF-8 derivatives: Impact of the substitution (Me, Cl, or Br) on imidazolate linker. *J. Phys. Chem. C* **2018**, *122*, 3846–3855.

[66] Desbiens, N.; Demachy, I.; Fuchs, A. H.; Kirsch-Rodeschini, H.; Soulard, M.; Patarin, J. Water condensation in hydrophobic nanopores. *Angew. Chem., Int. Ed.* **2005**, *44*, 5310–5313.

[67] Ortiz, G.; Nouali, H.; Marichal, C.; Chaplais, G.; Patarin, J. Energetic performances of "ZIF-71-aqueous solution" systems: A perfect shock-absorber with water. *J. Phys. Chem. C* **2014**, *118*, 21316–21322.

[68] Ortiz, G.; Nouali, H.; Marichal, C.; Chaplais, G.; Patarin, J. Versatile energetic behavior of ZIF-8 upon high pressure intrusion-extrusion of aqueous electrolyte solutions. *J. Phys. Chem. C* **2014**, *118*, 7321–7328.

[69] Sharma, M.; Wu, Y. D.; Car, R. *Ab initio* molecular dynamics with maximally localized wannier functions. *Int. J. Quantum Chem.* **2003**, *95*, 821–829.

[70] Soper, A. K.; Ricci, M. A. Structures of high-density and low-density water. *Phys. Rev. Lett.* **2000**, *84*, 2881–2884.

[71] Zhang, L.; Zheng, B.; Gao, Y.; Wang, L. L.; Wang, J. L.; Duan, X. B. Confined water vapor in ZIF-8 nanopores. *ACS Omega* **2022**, *7*, 64–69.

[72] Tang, F. J.; Li, Z. L.; Zhang, C. Y.; Louie, S. G.; Car, R.; Qiu, D. Y.; Wu, X. F. Many-body effects in the X-ray absorption spectra of liquid water. *Proc. Natl. Acad. Sci. USA* **2022**, *119*, e2201258119.

[73] Calero, S.; Gómez-Álvarez, P. Effect of the confinement and presence of cations on hydrogen bonding of water in LTA-type zeolite. *J. Phys. Chem. C* **2014**, *118*, 9056–9065.